Chemical Engineering Science 168 (2017) 391–402

Contents lists available at ScienceDirect

Chemical Engineering Science

journal homepage: www.elsevier.com/locate/ces

Analytical solutions for the free-draining flow of a Carreau-Yasuda fluid on a vertical plate

Juan Manuel Peralta *, Bárbara E. Meza, Susana E. Zorrilla

Instituto de Desarrollo Tecnológico para la Industria Química (INTEC), Universidad Nacional del Litoral-CONICET, Güemes 3450, S3000GLN, Santa Fe, Argentina

HIGHLIGHTS

- Analytical solutions of free-draining flow on a vertical plate were found.
- The flow was described by the Carreau-Yasuda rheological model.
- Solutions were partially validated with experimental data from literature.

GRAPHICAL ABSTRACT

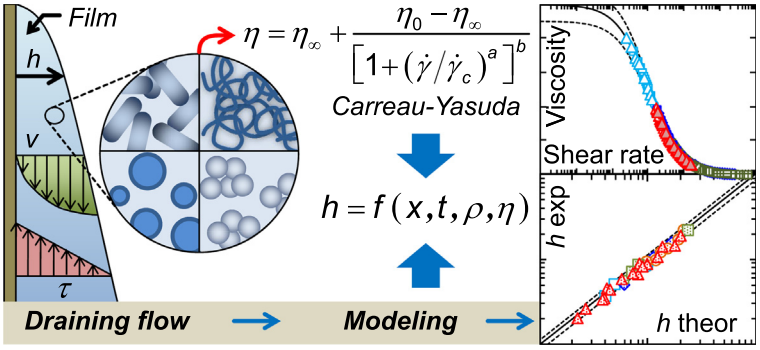

ARTICLE INFO

Article history:
Received 3 January 2017
Received in revised form 16 March 2017
Accepted 2 May 2017
Available online 4 May 2017

Keywords:
Free-draining
Coating
Carreau-Yasuda
Analytical solution

ABSTRACT

Free-draining flow is observed in many practical and industrial situations. It is considered as a stage of a batch dip-coating process, where the draining of the fluid will form a liquid film over a substrate by gravity. The objective of this work was to develop a mathematical model and to obtain analytical solutions for the fluid-dynamic variables of a free-draining flow during a dip-coating draining stage of a finite vertical plate using a fluid whose rheological behavior is described by the Carreau-Yasuda model. Mathematical expressions have been obtained assuming a monophasic, isothermal, and nonevaporative system, where the most important forces are viscous and gravitational. The studied phenomena occurred far away from the meniscus formed at the surface of the fluid reservoir. The main operative variables that were estimated are velocity profile, flow rate, local thickness, and average thickness of the film. A validation was performed by using experimental data of average film thickness values of several representative food-grade fluids with coating capacity (emulsions and suspensions) obtained from the literature. The information published in this work will be useful for researchers and technicians to control and predict film characteristics (thickness and uniformity) and operational variables (velocity and flow rate) during laboratory and industrial coating processes where free-draining flow takes place.

1. Introduction

Free-draining flow is observed in many practical and industrial situations, for example, during the drainage of liquids from tubes, reservoirs or tanks and as stage of a batch dip-coating process (Tallmadge and Gutfinger, 1967; Sherwood, 2009; Ungarish and Sherwood, 2012; Ali et al., 2016). The draining of the fluid that will form the coating over any substrate (long, short, rigid, flexible, porous, isolated, with regular or irregular shape) by gravity, is considered an important step for controlling the thickness and final

* Corresponding author.
E-mail address: jmperalta@intec.unl.edu.ar (J.M. Peralta).

http://dx.doi.org/10.1016/j.ces.2017.05.002
0009-2509/

Nomenclature

a, b	characteristic parameters used in Eq. (9)
Ca	capillary number $(\rho U \sigma^{-1})$
$\underline{e}_i$	unit vector in ith-direction
$\underline{F}_e$	external forces, N m^{-3}
${}_2F_1(\alpha, \beta; \delta; z)$	Gauss hypergeometric function
$\underline{g}$	gravity acceleration vector, m s^{-2}
g_x	gravity acceleration component, m s^{-2}
h	local film thickness, m
h_L	local film thickness at L, m
$\langle h \rangle_x$	area-averaged film thickness in the x-direction, m
L	length of the plate, m
K	consistency index, Pa s
n	behavior index
P	pressure, Pa
Q	flow rate per unit width, m^2 s^{-1}
St	Stokes number $\left(\rho g_x h_L^2 \eta_{ref}^{-1} U^{-1}\right)$
t	time, s
U	reference velocity in x-direction, m s^{-1}
v_i	velocity component in ith-direction, m s^{-1}
$\langle v_x \rangle_y$	area-averaged v_x in y-direction, m s^{-1}
x, y, z	Cartesian coordinates
$\underline{x}$	vector position, m
Z	normalized and dimensionless shear rate parameter
Z_m	normalized and dimensionless shear rate parameter evaluated at $y = 0$

Greek symbols

$\dot{\gamma}$	magnitude of the rate-of-strain, s^{-1}
$\dot{\gamma}_c$	characteristic rate-of-strain used in Eq. (9), s^{-1}
$\dot{\gamma}_m$	magnitude of the rate-of-strain evaluated at $y = 0$, s^{-1}
η	steady state viscosity, Pa s
η_0	limiting steady state viscosity when $\dot{\gamma} \to 0$ used in Eq. (9), Pa s
η_∞	limiting steady state viscosity when $\dot{\gamma} \to \infty$ used in Eq. (9), Pa s
η_c	shear-thinning relative viscosity defined in Eq. (21)
η_{ref}	steady state viscosity at reference state, Pa s
ξ	parameter defined as Z/Z_m
ρ	density, kg m^{-3}
σ	surface tension coefficient, N m^{-1}
τ_{ij}	viscous-stress tensor component acting in jth-direction on a plane with a normal vector acting in ith-direction, Pa
τ_0	yield stress, Pa

quality of films obtained during a dip-coating process (Tallmadge and Gutfinger, 1967; Schunk et al., 1997).

To understand the advantages and limitations of such process, it is important to have a fundamental understanding of the physical principles governing the fluid flow, including its rheological behavior. Sometimes, they can be expressed concisely though a mathematical model with a theoretical background. If an agreement between theory and experiment is established for the free-draining flow, the experimental data to explore the effect of process variables can be reduced. Therefore, the theoretical analysis often represents significant savings in time and money for assessing coating choices (Weinstein and Palmer, 1997). Indeed, analytical solutions provide a good alternative for solving mathematical models, because they are easier to obtain and use, less prone to error, and highly accurate (Sochi, 2015).

However, it is known that the connection between the transport phenomena governing the fluid flow and the rheological behavior of the fluid during any coating process is difficult to obtain using mathematical expressions (Eley and Schwartz, 2002). In recent years, our group has made efforts to find novel analytical solutions of mathematical models that describe the fluid-dynamic variables (like velocity and film thickness profiles) during the draining stage of a dip coating, incorporating to such expressions an equation that represents the rheological behavior of the fluid (Herschel-Bulkley, Power law, Casson, Quemada, etc.) (Peralta et al., 2014a; Peralta et al., 2014b; Peralta and Meza, 2016).

The Carreau-Yasuda model is a well-known rheological model used to estimate the steady state viscosity in a non-Newtonian fluid (Carreau, 1972; Yasuda, 1979). Recent studies have shown that it has a continuum mechanics foundation, albeit is considered an empirical rheological model (Surana, 2014). This expression was used to describe, in any of its forms and for certain conditions, the viscosity of several and different types of fluids (*e.g.* suspensions, emulsions, aerated emulsions, polymer solutions, and melts) (Lapasin and Pricl, 1995; Kistler and Schweizer, 1997; Dantzig and Tucker, 2001; Morrison, 2013; Osswald and Rudolph, 2014; Rao, 2014). Even though different phenomena may occur in these fluids, they have shown shear-thinning behavior in the range of conditions where Carreau-Yasuda model was used. Shear-thinning is a concept used to refer the viscosity decreasing due to an increment in the deformation rate applied to the fluid. It may be attributed to the dispersed and/or continuous-phase material (Genovese, 2012; Spikes and Jie, 2014) and can be described by assuming that fluids are dispersions of particles, where the main interactions are Brownian and hydrodynamic forces (Brummer, 2006). The shear-thinning region is observed when both forces are similarly relevant, achieved when the characteristic Peclet number (Pe) is $Pe = \mathcal{O}(1)$ (Quemada, 1998; Willenbacher and Georgieva, 2013). This approach simplifies the model and explains the viscosity variation for a fluid composition/structure and interactions (Quemada, 1998; Brummer, 2006; Willenbacher and Georgieva, 2013; Osswald and Rudolph, 2014).

Fig. 1 shows some examples of structural changes observed as consequence of shear rate variations in a shear-thinning fluid during a free-draining flow. As described in the literature (Quemada, 1998; Brummer, 2006; Willenbacher and Georgieva, 2013; Osswald and Rudolph, 2014), structurally viscous fluids may contain irregularly shaped particles, droplets or branched and/or entangled long molecular chains. In those systems, high levels of entropy are expected at rest and low rate of deformation due to a randomly distribution of particles as clusters of aggregates (high volume fractions) (Quemada, 1998; Genovese, 2012), droplets, and molecules. This highly structured fluid configuration exhibits a high constant viscosity value referred to as a Newtonian plateau (Osswald and Rudolph, 2014). At this point, the small deformation results in Brownian forces higher than its hydrodynamical counterpart ($Pe \ll 1$). Naturally, the system shows a tendency to maintain this state up to a point where further increments in shear rate (or shear stress) produce alignments of the structural components in the direction of the main flow. A disentanglement process, followed by a deformation of macromolecular chains and ellipsoidal deformed droplets, is observed for entangled molecular chains and emulsion droplets, respectively. Also, clusters, aggregates, and flocs tend to decompose into their elements (Quemada, 1998). In this range, the described phenomena leads to a shear-thinning behavior of the fluid, where Brownian and hydrodynamical forces are similar ($Pe = \mathcal{O}(1)$). Finally, as these structures tend to adopt less organized configurations and align in the direction of

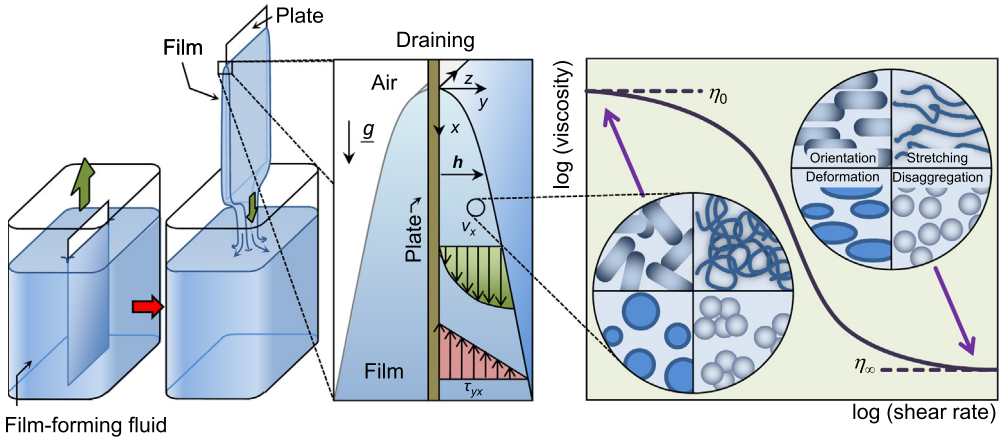

Fig. 1. Schematic representation of the main fluid-dynamic variables in the free-draining flow stage of a dip-coating process using a shear-thinning fluid. Details correspond to some effects of shear rate on fluid interaction and structures (*i.e.* orientation, stretching, deformation, and decay in aggregation).

the flow when the rate of deformation is increased, the system tends to flow more easily. Here, the high rate of deformation leads to large hydrodynamical interactions ($Pe \gg 1$). At this point, further increments in shear rate do not modify the configurations considered as fluid structures, and the viscosity tends to be constant again (second Newtonian plateau).

On one hand, even though numerous studies were focused on dip-coating systems using shear-thinning fluids, as far as the authors know only two of them used a Carreau or Carreau-Yasuda rheological models to predict the steady state viscosity (Javidi and Hrymak, 2015; Zhang et al., 2016). Furthermore, those studies were based on numerical and experimental work focused on systems where an asymptotic film thickness was formed due to balancing viscous and surface tension forces. The main phenomena occur around the fluid meniscus and are used to describe the formation of a thin film on a plate that is constantly withdrawn from a fluid bath. On the other hand, no theoretical studies for the draining stage (*i.e.* where usually the main forces are gravitational and viscous) of a dip-coating system using a Carreau-Yasuda model were found in the literature. Therefore, the objective of this work was to develop a mathematical model and to obtain analytical solutions for the fluid-dynamic variables of a free-draining flow during a dip-coating draining stage of a finite vertical plate using a fluid whose rheological behavior is described by the Carreau-Yasuda model.

2. Theoretical approach

2.1. Equations of change

A schematic representation of the free-draining flow stage of a dip-coating process is shown in Fig. 1. The figure indicates that the system studied in this work is similar to a previous published process (Peralta et al., 2014a; Peralta et al., 2014b; Peralta and Meza, 2016). Nevertheless, because of the nature of the constitutive model adopted further in the paper, a detailed description of all the steps used to achieve balances is essential to understand the obtained expressions for the main variables. Briefly, the studied phenomena occur far away from the meniscus (formed at the surface of the fluid reservoir), in isothermal and non-evaporative conditions. Also, the following assumptions were considered: (1) the fluid is incompressible ($\rho \neq f(\underline{x}, t)$), (2) the external forces are mainly gravitational ($\underline{F}_e = \rho \underline{g}$), (3) the surface interactions are negligible ($Ca \to \infty$), (4) the system is open ($\nabla P = 0$), (5) the system can be represented in Cartesian coordinates ($\underline{x} = \underline{e}_x x + \underline{e}_y y + \underline{e}_z z$), (6) the problem is mainly 2D (*i.e.* $\underline{v}_z \approx 0$ and changes in z direction are negligible: $\partial/\partial z \approx 0$), and (7) gravity acts in x-direction ($\underline{g} = \underline{e}_x g_x$),

$$\frac{\partial v_x}{\partial x} + \frac{\partial v_y}{\partial y} = 0 \tag{1}$$

$$\frac{\partial \tau_{yx}}{\partial y} \approx \rho g_x \tag{2}$$

$$\frac{\partial \tau_{xy}}{\partial x} + \frac{\partial \tau_{yy}}{\partial y} \approx 0 \tag{3}$$

Considering that the film will be surrounded at the top by air and that $\eta_{air} \ll \eta_{film}$, a feasible boundary condition will be $\tau_{yx} \approx 0$ in $y = h(x)$. Then, after integration, Eq. (2) yields:

$$\tau_{yx} = -\rho g_x (h - y) \tag{4}$$

This equation, as obtained and described in previous works (Peralta et al., 2014a; Peralta and Meza, 2016), predicts a linear profile of the shear stress across the film with a slope that depends on the ratio between gravitational and viscous forces. Also, it shows that τ_{yx} is independent on the fluid nature of the coating material (*i.e.* Newtonian, viscoelastic, etc.), and the maximum shear stress is expected at the plate surface: $\tau_m = -\rho g_x h$.

2.2. Range of theoretical validity of the approach

An important feature of the theoretical approach presented here is the verification of the range of validity of the set of Eqs. (1)–(3). As the system studied in this work is the same that was presented in previous studies (Peralta et al., 2014a; Peralta and Meza, 2016), the theoretical validity of the expressions presented can be made by checking the following expressions:

$$h_L / L \ll 1 \tag{5}$$

$$\frac{\rho U h_L^2}{\eta_{ref} L} \ll 1 \tag{6}$$

$$St = \frac{\rho g_x h_L^2}{\eta_{ref} U} = \mathcal{O}(1) \tag{7}$$

As stated in previous works (Peralta et al., 2014a; Peralta and Meza, 2016), it is noteworthy that in order to evaluate Eqs. (5)–(7), two parameters should be defined: (1) η_{ref} and (2) U. The definition of these parameters will depend on the adopted rheological model.

2.3. Constitutive equation

At this point, an additional equation that relates the rate of deformation (expressed as a function of the velocity gradients in the material) to the stress in the film is necessary. The simplest way to obtain this relationship is assuming the fluid material behavior as a generalized Newtonian fluid:

$$\underline{\underline{\tau}} = -\eta\underline{\underline{\dot{\gamma}}} \tag{8}$$

where $\underline{\underline{\tau}}$ is the viscous stress tensor [Pa], η is the steady state viscosity [Pa s], and $\underline{\underline{\dot{\gamma}}}$ is the rate-of-strain tensor [s^{-1}]. Here, η is a function of the magnitude of the viscous stress tensor τ or the magnitude of the rate-of-strain tensor $\dot{\gamma}$, temperature, pressure, and concentration.

The rheological model used to estimate η as a function of $\dot{\gamma}$ is the well-known shear-thinning Carreau-Yasuda model (Carreau, 1972; Yasuda, 1979):

$$\eta = \eta_\infty + \frac{\eta_0 - \eta_\infty}{\left[1 + (\dot{\gamma}/\dot{\gamma}_c)^a\right]^b} \tag{9}$$

where η_∞ is the limiting steady state viscosity when $\dot{\gamma} \to \infty$ (*i.e.* $\lim_{\dot{\gamma}\to\infty}\eta$) [Pa s], η_0 is the limiting steady state viscosity when $\dot{\gamma} \to 0$ (*i.e.* $\lim_{\dot{\gamma}\to 0}\eta$) [Pa s], $\dot{\gamma}_c$ is a characteristic shear rate [s^{-1}], and a and b are characteristic parameters. These parameters could be described as a function of system variables such as concentration, temperature, and pressure (Osswald and Rudolph, 2014).

It is important to mention that several well-known rheological models can be obtained by modifying conveniently the parameters in Eq. (9). Some of these models were listed elsewhere with modifications in their derivations (Osswald and Rudolph, 2014): **Carreau model** (Carreau, 1972), $a = 2$ then $\eta = \eta_\infty + (\eta_0 - \eta_\infty)/[1+(\dot{\gamma}/\dot{\gamma}_c)^2]^b$; **Cross model** (Cross, 1965), $b = 1$ then $\eta = \eta_\infty + (\eta_0 - \eta_\infty)/[1 + (\dot{\gamma}/\dot{\gamma}_c)^a]$; **Bingham model** (Bingham, 1922), $a = b = -1, \eta_0 = K, (\eta_0 - \eta_\infty)\dot{\gamma}_c = \tau_0$ then $\eta = K + \tau_0/\dot{\gamma}$; and **Ostwald-de Waele model** (*i.e.* Power law) (Ostwald, 1925), $a = 1, b = 1 - n, \dot{\gamma} \gg \dot{\gamma}_c, \eta_0 \gg \eta_\infty, \eta_0/\dot{\gamma}_c = K$ then $\eta \approx K\dot{\gamma}^{n-1}$.

Although analytical solutions were found in previous studies using Cross, Bingham, and Ostwald-deWaele fluids for a similar dip-coating draining stage (Peralta et al., 2014a; Peralta and Meza, 2016), new solutions using Carreau-Yasuda and Carreau fluids will be presented in the following Sections. This generality feature of Eq. (9) increases the practical application of the present study.

At this point, it would be helpful to show briefly the effect of the parameters of Eq. (9) on the viscosity estimation. Fig. 2 shows predicted steady state viscosity profiles as a function of shear rate obtained by Eq. (9) for a shear-thinning fluid (*i.e.* $\eta_0 > \eta_\infty$) and selected values of $\eta_0, \eta_\infty, \dot{\gamma}_c, a$, and b. First, as η_0 and η_∞ are the limits of the range of possible viscosity values predicted by Eq. (9), variations in those parameters vertically scale the profiles. Second, $\dot{\gamma}_c$ is related to a characteristic response time (inverse) of the fluid and changes in this parameter produce a horizontal shift in the profile. For example, in dispersions $\dot{\gamma}_c$ is related to the mean particle size in the fluid, being higher for smaller particles (Willenbacher and Georgieva, 2013; Morrison, 2013). When $\dot{\gamma} = \dot{\gamma}_c$, viscosity is $\eta = (\eta_0 + \eta_\infty)/2$. Third, a and b primarily affect the slope of the thinning range of viscosity. The main difference is that a produces these slope changes pivoting at $\dot{\gamma}_c$ and controls the curvature of the concave region (Morrison, 2013; Osswald and Rudolph, 2014), while b has an asymmetric effect on the entire profile. The combined effect of these parameters gives Eq. (9) the freedom of different profile curvatures near η_0 and η_∞, resulting in a highly descriptive capability of Eq. (9) to experimental data compared to simpler models.

Now, two magnitudes are required to be calculated to continue with the analysis: $\dot{\gamma}$ and τ. This calculation can be carried out applying a dimensional analysis to the definition of the rate-of-strain and viscous stress tensors. That is, $\underline{\underline{\dot{\gamma}}} = \underline{\nabla v} + (\underline{\nabla v})^T$ where $\dot{\gamma}_{ij} = \partial v_i/\partial x_j + \partial v_j/\partial x_i$ and, according to Eq. (2), the only component of $\underline{\underline{\tau}}$ necessary to calculate is $\tau_{yx} = -\eta(\partial v_y/\partial x + \partial v_x/\partial y)$. Finally, after applying the dimensional analysis presented in a previous work (Peralta and Meza, 2016):

$$\dot{\gamma} \approx \left|\frac{\partial v_x}{\partial y}\right| \tag{10}$$

$$\tau_{yx} \approx -\eta\frac{\partial v_x}{\partial y} \tag{11}$$

Henceforth, to simplify the presentation of the equations, approximately equal signs will be replaced by equal signs.

2.4. Velocity profile

Taking into account Eqs. (4) and (11), the fluid velocity profile (*i.e.* the velocity component in x-direction) can be estimated by:

$$v_x = \int_{\dot{\gamma}_m}^{\dot{\gamma}} \frac{\dot{\gamma}}{(\partial\dot{\gamma}/\partial y)}\,d\dot{\gamma} \tag{12}$$

where $\dot{\gamma}_m$ is the shear rate obtained at the plate surface. Now, the denominator of Eq. (12) can be rearranged by the resulted expression of replacing the velocity gradient in Eq. (11) with $\dot{\gamma}$ (Eq. (10)) and differentiating with respect to y, to yield:

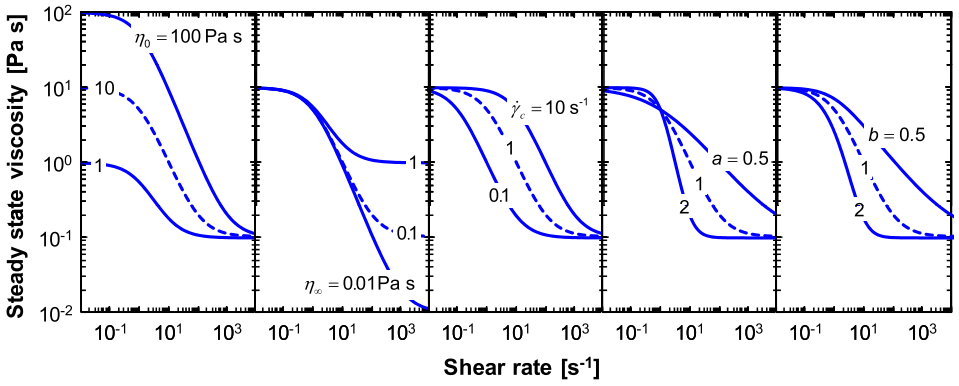

Fig. 2. Steady state viscosity profiles as a function of shear rate predicted by Eq. (9) for selected values of η_0, η_∞, $\dot{\gamma}_c$, a, and b. Dashed lines represent a reference condition with $\eta_0 = 10$ Pa s, $\eta_\infty = 0.1$ Pa s, $\dot{\gamma}_c = 1\ s^{-1}$, and $a = b = 1$.

$$v_x = \int_{\dot{\gamma}_m}^{\dot{\gamma}} \frac{\dot{\gamma}}{(\partial\tau/\partial y)}\left[\eta + \dot{\gamma}\frac{\partial\eta}{\partial\dot{\gamma}}\right]d\dot{\gamma} \tag{13}$$

As $\dot{\gamma}$ and $\dot{\gamma}_m$ can theoretically range from 0 to ∞, a convenient way to handle this feature is to define a normalized and dimensionless shear rate parameter, that ranges from 0 to 1, as:

$$Z = \frac{(\dot{\gamma}/\dot{\gamma}_c)^a}{1+(\dot{\gamma}/\dot{\gamma}_c)^a} \tag{14}$$

Replacing the derivative of Eq. (4) with respect to y in the denominator of Eq. (13) and using Z to change variables: $\dot{\gamma} = \dot{\gamma}_c Z^{1/a}/(1-Z)^{1/a}$, $\partial\dot{\gamma}/\partial Z = (\dot{\gamma}_c/a)Z^{1/a-1}/(1-Z)^{1/a-1}$, $\partial\eta/\partial Z = -b(\eta_0-\eta_\infty)(1-Z)^{b-1}$, and $\eta = \eta_0[\eta_c + (1-\eta_c)(1-Z)^b]$, the velocity can be expressed as:

$$v_x = \frac{\eta_0\dot{\gamma}_c^2}{\rho g_x}\int_Z^{Z_m}\left[\frac{\eta_c}{a} + \frac{(1-\eta_c)}{a(1-Z)^{-b}} - \frac{b(1-\eta_c)Z}{(1-Z)^{-b}}\right]\frac{Z^{2/a-1}}{(1-Z)^{2/a+1}}dZ \tag{15}$$

where $Z_m = (\dot{\gamma}_m/\dot{\gamma}_c)^a/[1+(\dot{\gamma}_m/\dot{\gamma}_c)^a]$ and $\eta_c = \eta_\infty/\eta_0$.

To integrate Eq. (15) the following identities can be used (Weisstein, 2016a; Weisstein, 2016b):

$$\int_0^Z \frac{Z^A}{(1-Z)^{-B}}dZ = \frac{Z^A(1-Z)^B}{A}{}_2F_1(1, A+B; A+1; Z) \tag{16}$$

$${}_2F_1(1, A+B+1; A+2; Z) = \frac{A+1}{A+B}Z^{-1}[{}_2F_1(1, A+B; A+1; Z) - 1] \tag{17}$$

where Eq. (16) is the Chebyshev integral, in terms of the Gauss hypergeometric function ${}_2F_1(\alpha,\beta;\delta;x)$, and holds when $-A$ is not a natural number.

Finally, applying Eqs. (16) and (17) to Eq. (15), the expression for the velocity profile in the film is:

$$v_x = \frac{\eta_0\dot{\gamma}_c^2}{2\rho g_x}[\psi(\dot{\gamma}_m) - \psi(\dot{\gamma})] \tag{18}$$

$$\psi(\dot{\gamma}_m) = \frac{Z_m^{2/a}}{(1-Z_m)^{2/a}}\left\{\eta_c + (1-\eta_c)(1-Z_m)^b\left[2 - {}_2F_1\left(1, b; \frac{2}{a}+1; Z_m\right)\right]\right\} \tag{19}$$

$$\psi(\dot{\gamma}) = \frac{Z^{2/a}}{(1-Z)^{2/a}}\left\{\eta_c + (1-\eta_c)(1-Z)^b\left[2 - {}_2F_1\left(1, b; \frac{2}{a}+1; Z\right)\right]\right\} \tag{20}$$

$$\eta_c = \frac{\eta_\infty}{\eta_0} \tag{21}$$

It is noteworthy to mention that v_x is a function of $\dot{\gamma}$ in Eqs. (18)–(21). That is, a set of parametric equations are necessary to relate v_x with the position y. This can be done by combining Eqs. (4) and (9)–(11), and defining $\xi = Z/Z_m$ to obtain:

$$\frac{y}{h} = 1 - \frac{\left[\eta_c + (1-\eta_c)(1-\xi Z_m)^b\right]\xi^{1/a}(1-Z_m)^{1/a}}{\left[\eta_c + (1-\eta_c)(1-Z_m)^b\right](1-\xi Z_m)^{1/a}} \tag{22}$$

Now, the velocity profile can be calculated by giving values to ξ from 0 (*i.e.* air-film interface) to 1 (*i.e.* plate-film interface) to obtain v_x vs. y/h.

2.5. Flow rate

The flow rate per unit with of the plate can be estimated by:

$$Q = \int_0^h v_x dy \tag{23}$$

taking into account Eq. (14), evaluated at the plate-film interface (*i.e.* Z_m), to change variables and Eqs. (16)–(21) to integrate Eq. (23), the expression of Q for a Carreau-Yasuda fluid is:

$$\begin{aligned} Q = \frac{\eta_0^2\dot{\gamma}_m^3}{3(\rho g_x)^2}\Bigg[&\eta_c^2 + \frac{2\eta_c(1-\eta_c)}{(1-Z_m)^{-b}}{}_2F_1\left(1, b; \frac{3}{a}+1; Z_m\right) \\ &+ (1-\eta_c)^2(1-Z_m)^{2b}{}_2F_1\left(1, 2b; \frac{3}{a}+1; Z_m\right) \\ &- \frac{3ab\eta_c(1-\eta_c)Z_m}{(3+a)(1-Z_m)^{-b}}{}_2F_1\left(1, b+1; \frac{3}{a}+2; Z_m\right) \\ &- \frac{3ab(1-\eta_c)^2Z_m}{(3+a)(1-Z_m)^{-2b}}{}_2F_1\left(1, 2b+1; \frac{3}{a}+2; Z_m\right)\Bigg] \end{aligned} \tag{24}$$

Additionally, the area-averaged (in y-direction) fluid velocity at position x can be estimated by knowing that: $\langle v_x\rangle_y = Q/h$.

2.6. Local film thickness

Considering the assumptions made in previous Sections, a mass balance on the film in terms of h yields (Peralta et al., 2014a; Peralta and Meza, 2016):

$$\frac{\partial h}{\partial t} + \frac{\partial Q}{\partial x} = 0 \tag{25}$$

Assuming that $h = 0$ at $x = 0$ (*i.e.* at the beginning of the coated plate) for $t > 0$ and monotonicity of Q on h (for simplicity), the solution to Eq. (25) can be written as (Peralta et al., 2014a; Peralta and Meza, 2016):

$$\frac{x}{t} = \frac{\partial Q}{\partial h} \tag{26}$$

To find an expression for h, the derivative of Eq. (26) is: $\partial Q/\partial h = (\partial Q/\partial Z_m)(\partial Z_m/\partial\dot{\gamma}_m)(\partial\dot{\gamma}_m/\partial\eta_m)(\partial\eta_m/\partial h)$. Now, using Eqs. (4), (9), (10), (11), and (14) evaluated at the plate-film interface (*i.e.* Z_m), the local film thickness can be calculated by:

$$\left[h^a + \frac{(x/t)^a}{\dot{\gamma}_c^a}\right]^b\frac{\rho g_x h^2}{(x/t)} - \left[h^a + \frac{(x/t)^a}{\dot{\gamma}_c^a}\right]^b\eta_\infty - (\eta_0-\eta_\infty)h^{ab} = 0 \tag{27}$$

2.7. Average film thickness

As stated in previous works (Peralta et al., 2014a; Peralta and Meza, 2016), the uniformity of the film is one of the main properties to be evaluated in a coating process. This quantity can be estimated by the ratio of the average film thickness to the local thickness at any time and position (Gutfinger and Tallmadge, 1965). Consequently, the uniformity ranges from 1/2 to 1 for any given position x, obtaining more leveled films as this parameter tend to 1 and vice versa.

The average film thickness at a distance x can be calculated as an area-averaged parameter as:

$$\langle h\rangle_x = \frac{1}{x}\int_0^x h dx \tag{28}$$

To integrate Eq. (28), a change of variables using the local film thickness profile (Eq. (27)) combined with Eq. (14) evaluated at the plate-film interface (*i.e.* Z_m) is necessary. Then, an expression for $h = f(Z_m)$ is found using the relation $\rho g_x h = \eta_m\dot{\gamma}_m$ with Eqs. (9) and (14) evaluated at Z_m (Gutfinger and Tallmadge, 1965; Peralta et al., 2014a; Peralta and Meza, 2016). Subsequently, Eq. (28) can be written as:

$$\frac{\langle h\rangle_x}{h}=\frac{Z_m^{-2/a}(1-Z_m)^{2/a}}{a\left[\eta_c+(1-\eta_c)(1-Z_m)^b\right]^2}\left[2\eta_c^2\int_0^{Z_m}\frac{Z_m^{3/a-1}}{(1-Z_m)^{3/a+1}}dZ_m+4\eta_c(1-\eta_c)\int_0^{Z_m}\frac{Z_m^{3/a-1}}{(1-Z_m)^{3/a-b+1}}dZ_m+2(1-\eta_c)^2\int_0^{Z_m}\frac{Z_m^{3/a-1}}{(1-Z_m)^{3/a-2b+1}}dZ_m-ab\eta_c(1-\eta_c)\int_0^{Z_m}\frac{Z_m^{3/a}}{(1-Z_m)^{3/a-b+1}}dZ_m-ab(1-\eta_c)^2\int_0^{Z_m}\frac{Z_m^{3/a}}{(1-Z_m)^{3/a-2b+1}}dZ_m\right] \quad (29)$$

Now, using Eq. (16), the uniformity can be estimated by:

$$\frac{\langle h\rangle_x}{h}=\frac{1}{\left[\eta_c+(1-\eta_c)(1-Z_m)^b\right]^2}\left[\frac{2}{3}\eta_c^2+\frac{4\eta_c}{3}\frac{(1-\eta_c)}{(1-Z_m)^{-b}}{}_2F_1\left(1,b;\frac{3}{a}+1;Z_m\right)+\frac{2}{3}(1-\eta_c)^2(1-Z_m)^{2b}{}_2F_1\left(1,2b;\frac{3}{a}+1;Z_m\right)-\frac{ab(1-\eta_c)^2Z_m}{(3+a)(1-Z_m)^{-2b}}{}_2F_1\left(1,2b+1;\frac{3}{a}+2;Z_m\right)-\frac{ab\eta_c(1-\eta_c)Z_m}{(3+a)(1-Z_m)^{-b}}{}_2F_1\left(1,b+1;\frac{3}{a}+2;Z_m\right)\right] \quad (30)$$

2.8. Validation

A partial experimental validation was carried out to test the capabilities of the mathematical model developed in this work. Experimental data (steady shear viscosity and average film thickness values) of several representative fluids were obtained from literature. As the calculation of the film thickness must take into account the correct representation of viscosity, the ability of Eq. (9) to describe the rheological behavior of several type of materials by fitting viscosity experimental data and the ability of Eq. (30) to predict experimental average film thickness were tested.

2.8.1. Experimental data

Rheological properties, density, and average film thickness values of several food-grade fluids with coating capacity obtained from literature were used (Table 1): (1) a commercial pasteurized milk cream emulsion (substrate: glass plates, L = 40 mm, draining times: 10 and 30 s) (Peralta and Meza, 2016), (2) a condensed sweet milk suspension (substrate: glass plates, L = 40 mm, draining times: 5, 10, 30, and 60 s) (Peralta and Meza, 2016), (3) a microparticulated whey protein suspension (MWPS) with 30% total solids content (substrate: glass plates, L = 40 mm, draining time: 30 s) (Peralta and Meza, 2016), (4) a commercial food glaze suspension (substrate: glass plates, L = 40 mm, draining time: 30 s) (Meza et al., 2015), (5) a milk chocolate with different percentages of lecithin and polyglycerol (substrate: acrylic plates, L = 44.5 mm, draining time: 20 s) (Karnjanolarn and Mccarthy, 2006), and (6) six trademarks of deep-fat frying commercial batters (substrate: polymethyl methacrylate plates, L = 40 mm, draining times: 60 and 120 s, mixing: 270–300 rpm for 3–4 min) (Lee et al., 2002). The theoretical values of h and $\langle h\rangle_x$ were calculated at L and t corresponding to the draining times.

Table 1
Physical properties and rheological parameters fitted to Eq. (9) of food-grade fluids with coating capacity obtained from the literature.

Fluid	$\dot{\gamma}$ [s^{-1}]	τ [Pa]	ρ [kg m^{-3}]	η_0 [Pa s]	η_∞ [Pa s]	$\dot{\gamma}_c$ [s^{-1}]	a [–]	b [–]	Error[h] [%]
C[a]	0.2–6	7–19	986	175.20	1.47	0.0426	2.00	0.46	1.29
CM[b]	0.2–3	1–18	1367	8.81	3.05	0.1182	1.90	0.12	0.11
MWPS[c]	0.4–192	0.1–12	1088	0.31	0.01	0.7354	1.30	0.26	1.67
G20[d]	0.6–13	30–202	1336	247.29	0.79	0.0113	1.93	0.21	2.86
G30[d]	0.6–50	14–255	1334	116.19	0.70	0.0118	1.94	0.20	3.37
G40[d]	0.6–50	9–162	1331	66.39	0.62	0.0123	1.95	0.20	2.46
G50[d]	0.6–50	4–108	1327	31.35	0.55	0.0127	1.96	0.19	5.38
MCL0[e]	1.9–50	50–333	1216	1147.98	11.48	0.0039	1.24	0.45	4.29
MCL0.1[e]	1.9–50	22–196	1216	924.27	5.66	0.0072	1.41	0.46	2.36
MCL0.2[e]	1.9–50	16–161	1216	585.40	4.23	0.0113	1.59	0.44	1.51
MCL0.3[e]	1.9–50	15–125	1216	401.41	3.73	0.0184	1.78	0.42	1.30
MCL0.4[e]	1.9–50	15–128	1216	298.93	2.98	0.0333	2.03	0.38	2.04
MCL0.5[e]	1.9–50	15–125	1216	159.99	1.97	0.0417	2.30	0.36	2.09
MCP0.1[f]	1.9–50	31–297	1216	898.51	9.61	0.0040	1.36	0.47	1.70
MCP0.2[f]	1.9–50	17–248	1216	532.82	9.00	0.0041	1.48	0.51	1.99
MCP0.3[f]	1.9–50	12–230	1216	346.50	7.47	0.0042	1.62	0.51	5.35
MCP0.4[f]	1.9–50	9–219	1216	239.81	5.74	0.0043	1.77	0.49	7.42
MCP0.5[f]	1.9–50	8–241	1216	200.00	4.14	0.0044	1.93	0.47	2.96
BDD[g]	0.1–50	2–82	1160	26.87	0.48	0.0435	1.17	0.37	1.41
BD[g]	0.1–50	2–79	1140	28.14	0.50	0.0397	0.75	0.60	1.22
BGD[g]	0.1–50	14–464	1160	160.32	1.00	0.0540	1.00	0.43	0.94
BK[g]	0.1–50	6–120	1140	92.62	2.10	0.0457	0.92	0.55	1.25
BTI[g]	0.1–50	9–197	1150	98.71	0.82	0.0533	0.96	0.42	1.00
BNW[g]	0.1–50	5–73	1110	64.02	0.68	0.0507	1.20	0.42	0.85

[a] Cream (T = 20 °C) (Peralta and Meza, 2016).
[b] Condensed milk (T = 20 °C) (Peralta and Meza, 2016).
[c] Microparticulated whey protein suspension (T = 20 °C, C = 30%) (Peralta and Meza, 2016).
[d] Glaze suspension (GXX, XX = 20, 30, 40, 50 °C) (Meza et al., 2015).
[e] Milk chocolate + lecithin (T = 20 °C, MCLX.X, X.X = 0, 0.1, 0.2, 0.3, 0.4, 0.5%) (Karnjanolarn and Mccarthy, 2006).
[f] Milk chocolate + polyglycerol (T = 20 °C, MCPX.X, X.X = 0, 0.1, 0.2, 0.3, 0.4, 0.5%) (Karnjanolarn and Mccarthy, 2006).
[g] Batter (T = 20 °C, C = 50%, BDD = Dorothy Dawson, BD = Drakes, BGD = Golden dipt, BK = Kikkoman, BTI = Tung-I, BNW = Newly wed) (Lee et al., 2002).
[h] *MAPE* using Eq. (31) for steady state viscosity data.

2.8.2. Validation procedure

The five parameters of Eq. (9) were found simultaneously using the viscosity data for each studied fluid by minimizing the mean absolute percentage error (*MAPE*):

$$MAPE = \frac{100}{N}\sum_{i=1}^{N}\sqrt{\left(1-\frac{a_{i,theor}}{a_{i,exp}}\right)^2} \tag{31}$$

where N is the number of steady state viscosity data points of each food-grade fluid (Table 1) and $a_{i,theor}$ and $a_{i,exp}$ are the theoretical and experimental values of η, respectively. Then, to conveniently display and compare experimental and theoretical viscosity values, the viscosity data were rearranged as reduced viscosity η^* using:

$$\eta^* = \left(\frac{\eta-\eta_\infty}{\eta_0-\eta_\infty}\right)^{1/b} = \frac{1}{1+(\dot\gamma/\dot\gamma_c)^a} = \frac{1}{1+\Gamma} \tag{32}$$

where Γ is a dimensionless shear rate parameter defined as $(\dot\gamma/\dot\gamma_c)^a$.

Similarly, the prediction capability of the model to experimental values of $\langle h\rangle_x$ was evaluated using Eq. (31). In this case, N is the number of food-grade fluids (Table 1) and $a_{i,theor}$ and $a_{i,exp}$ are the theoretical and experimental values of $\langle h\rangle_x$ estimated with Eq. (30), respectively.

3. Results and discussion

3.1. Theoretical range of validity

As stated above and following the rationale presented in previous works (Peralta et al., 2014a; Peralta and Meza, 2016), some assumptions are necessary for obtaining simpler and useful forms of Eqs. (5)–(7). First, a natural and conservative way to estimate U

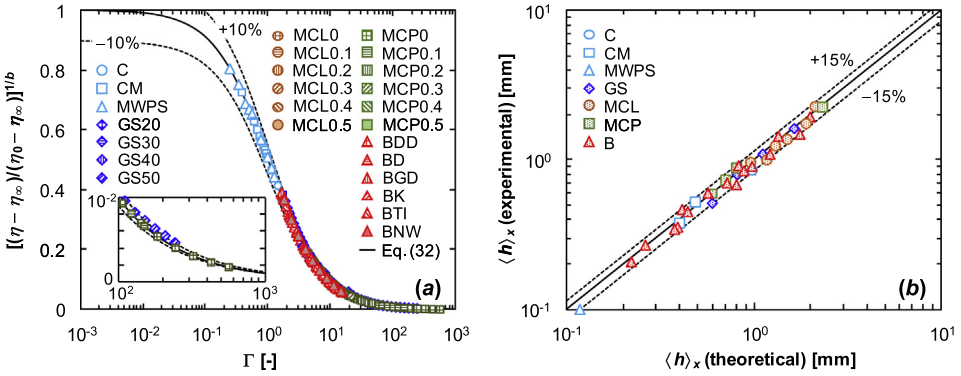

Fig. 3. (a) Reduced viscosity data fitted to Eq. (32), and (b) comparison between experimental (symbols) and theoretical (solid lines) values of $\langle h\rangle_x$ for food-grade fluids with coating capacity (Table 1). Dashed lines correspond to an error of (a) 10% and (b) 15%.

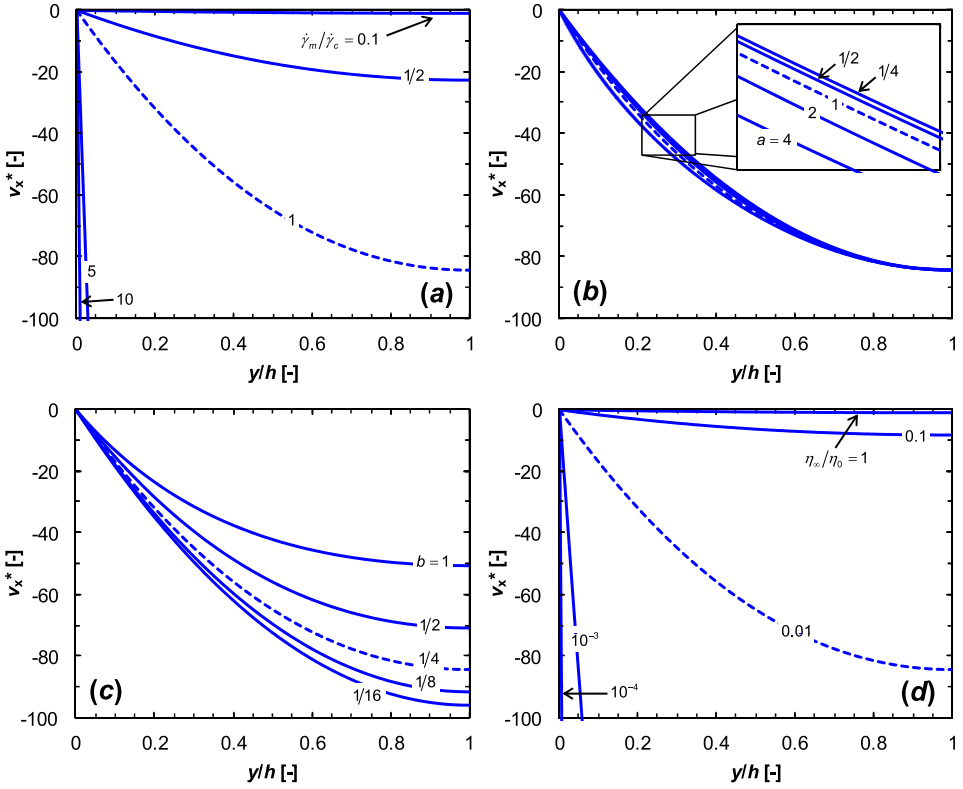

Fig. 4. Dimensionless velocity profiles as a function of the dimensionless position y/h for selected values of: (a) $\dot\gamma_m/\dot\gamma_c$, (b) a, (c) b, and (d) η_∞/η_0. Dashed lines represent a reference condition with $\dot\gamma_m/\dot\gamma_c = 1$, $a = 1$, $b = 1/4$, and $\eta_\infty/\eta_0 = 0.01$.

is defining $St = 1$ from Eq. (7) to get $U = \rho g_x h_L^2/\eta_{ref}$. That is, the gravitational and viscous forces are equal in magnitude. Second, for a shear-thinning fluid, the most conservative way to define the reference viscosity could be $\eta_{ref} = \eta_\infty$ because it is the minimum value that viscosity would adopt. Conversely, $\eta_{ref} = \eta_0$ can be set for a shear-thickening fluid. Therefore, the range of validity of the present model (shear-thinning) can be verified by checking simultaneously Eq. (5) and:

$$\frac{g_x \rho^2 h_L^3}{\eta_\infty^2} \leqslant 1 \tag{33}$$

It is noteworthy to note that Eq. (33) was obtained from very restrictive assumptions and the applicability of the model to data that falls outside the range proposed by this equation should be tested with Eqs. (5)–(7).

3.2. Experimental validation

The agreement between experimental and theoretical reduced viscosity values predicted by Eq. (32) for the food-grade fluids with coating capacity is shown in Fig. 3a. Good correspondence is observed for a wide range of $(\dot\gamma/\dot\gamma_c)^a$ (*i.e.* dimensionless shear rate), with *MAPE* values (Eq. (31)) showing errors less than 10% (Table 1). This feature exhibits a great description capability of the Carreau-Yasuda model (Eq. (9)) when applied to several type of dispersions (*i.e.* suspensions, emulsions, aerated suspensions, etc.) at different operational conditions (temperature, ingredient concentrations, mixing, etc.) and for a wide range of shear rates (Osswald and Rudolph, 2014). Also, it is noteworthy to mention that the significance of the experimental validation carried out in this study can be considered acceptable due to the wide range of the rheological parameters obtained by Eq. (9): 0.31 Pa s $\leqslant \eta_0 \leqslant$1147.98 Pa s,

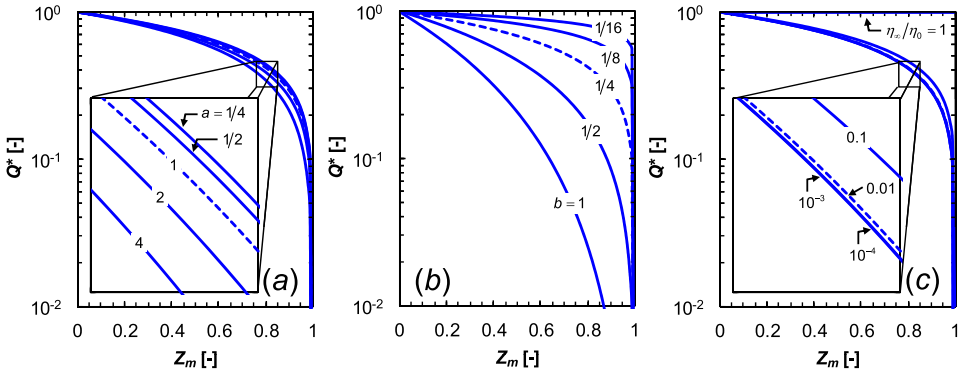

Fig. 5. Dimensionless flow rate as a function of the normalized and dimensionless shear rate parameter for selected values of: (a) a, (b) b, and (c) η_∞/η_0. Dashed lines represent a reference condition with $a = 1$, $b = 1/4$, and $\eta_\infty/\eta_0 = 0.01$.

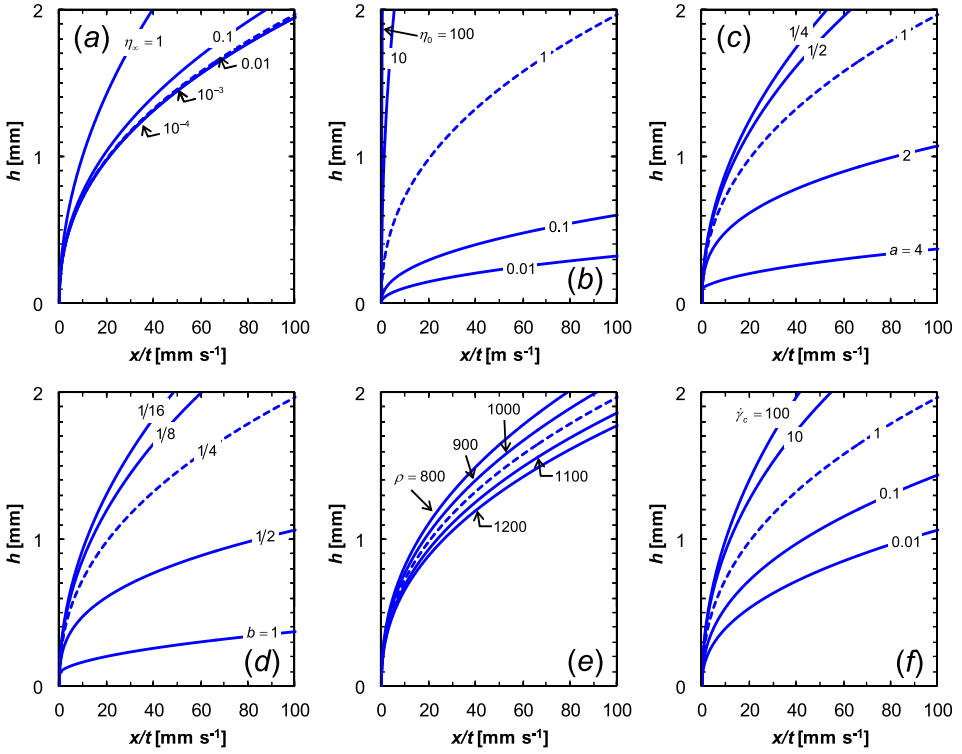

Fig. 6. Local film thickness as a function of the space-time variable x/t for selected values of (a) η_∞, (b) η_0, (c) a, (d) b, (e) ρ, and (f) $\dot\gamma_c$. Dashed lines represent a reference condition with $\eta_\infty = 10^{-2}$ Pa s, $\eta_0 = 1$ Pa s, $a = 1$, $b = 1/4$, $\rho = 1000$ kg m^{-3}, and $\dot\gamma_c = 1$ s^{-1}.

$0.01\ \text{Pa s} \leqslant \eta_\infty \leqslant 11.48\ \text{Pa s}$, $0.0039\ \text{s}^{-1} \leqslant \dot{\gamma}_c \leqslant 0.7354\ \text{s}^{-1}$, $0.92 \leqslant a \leqslant 2.30$, and $0.12 \leqslant b \leqslant 0.60$. Table 1 shows that in general, η_0 and η_∞ decreased as temperature and plasticizer concentration (*i.e.* lecithin and polyglycerol) increased. The opposite behavior is observed for $\dot{\gamma}_c$. In the case of η_0 and η_∞, an increase in temperature produces an increase in the thermal energy of molecules giving them more chance to move. Also, an increase in the plasticizer concentration dilutes the dispersion and produces a less viscous continuous phase, resulting in a less viscous dispersion (Osswald and Rudolph, 2014; Rao, 2014). In the case of $\dot{\gamma}_c$ and for dispersions, the Peclet number gives the following relation $\dot{\gamma}_c \propto T/\eta_f$, where η_f is the viscosity of the continuous phase. Therefore, an increase in T would produce a decrease in η_f, resulting in an increase in $\dot{\gamma}_c$. The prediction capability of Eq. (30) to experimental average film thickness can be seen in Fig. 3b. Again, good and consistent agreement ($MAPE < 15\%$) is observed for values ranging from 0.1 mm to 10 mm. All the data, from very thin to very thick films, were reasonably predicted by the model. This level of agreement was also observed in previous works (Peralta et al., 2014b; Peralta and Meza, 2016).

3.3. Sensitivity analysis

Briefly, a sensitivity analysis is performed to show a representative response of Eqs. (18)–(22), (24), (27), and (30) to selected values of the main physical and model parameters. All profiles were obtained for a shear-thinning fluid (*i.e.* $\eta_0 > \eta_\infty$). New evaluations would be needed assuming a shear-thickening fluid, as an irregular response of the effect of the parameters on the main variables can be expected.

3.3.1. Velocity profiles

Fig. 4 shows dimensionless velocity profiles ($v_x^* = 2v_x\rho g_x/(\eta_0\dot{\gamma}_c^2)$) as a function of y/h for selected values of $\dot{\gamma}_m/\dot{\gamma}_c, a, b$, and η_∞/η_0. First, an increase in $\dot{\gamma}_m/\dot{\gamma}_c$ produces an increase in velocity (Fig. 4a). That is, the lower boundary of the range of local viscosity values adopted by the film approaches to η_∞. Therefore, the fluid is overall and relatively less viscous and drain more easily. Also, due to the range that $\dot{\gamma}_m/\dot{\gamma}_c$ can vary is practically large, its effect on η can be also important. Second, an increment in a produces an increment in v_x^* (Fig. 4b). In this case, the effect is less pronounced compared to $\dot{\gamma}_m/\dot{\gamma}_c$. This is partially due to the range of a selected for the analysis (range that a usually varies) and also to the fact that this fitting parameter produces smaller changes in the viscosity profile. Third, an increase in b produces smaller velocity profiles (Fig. 4c). That is, the thinning effect of the shear rate on viscosity (Eq. (9)) is increased. An increase in b does not only produce more stepped viscosity (as in the case of a) profiles but also contributes to shift the position of the transition from η_0 to η_∞ more markedly than a. Fourth, as η_∞/η_0 decreases, the film becomes relatively more viscous and tends to flow less (Fig. 4d). This parameter, along with $\dot{\gamma}_m/\dot{\gamma}_c$, is the most important to explain changes in velocity profiles.

3.3.2. Flow rate

The effect of the normalized and dimensionless shear rate parameter evaluated at the plate wall (Z_m) on the dimensionless flow rate per unit with $Q^* = 3(\rho g_x)^2 Q/(\eta_0^2\dot{\gamma}_m^3)$ for selected values of a, b, and η_∞/η_0 is shown in Fig. 5. Here, Q^* is calculated relative to the flow rate obtained when $\eta = \eta_0$, so profiles show concave shapes and change from $Q^* = 1$ at $Z_m = 0$ to $Q^* = \eta_c^2$ at $Z_m = 1$. This leads to calculate, at the extremes of profiles (*i.e.* Newtonian plateaus in Eq. (9)), dimensional flow rates as $Q = \rho g_x h^3/(3\eta_0)$ and $Q = \rho g_x h^3/(3\eta_\infty)$. On one hand, an increment in a produces less concave profiles and consequently lower values of Q^* (Fig. 5a). The same overall effect is observed in the case of b (Fig. 5b). However, same increments in a and b produce larger changes in profiles

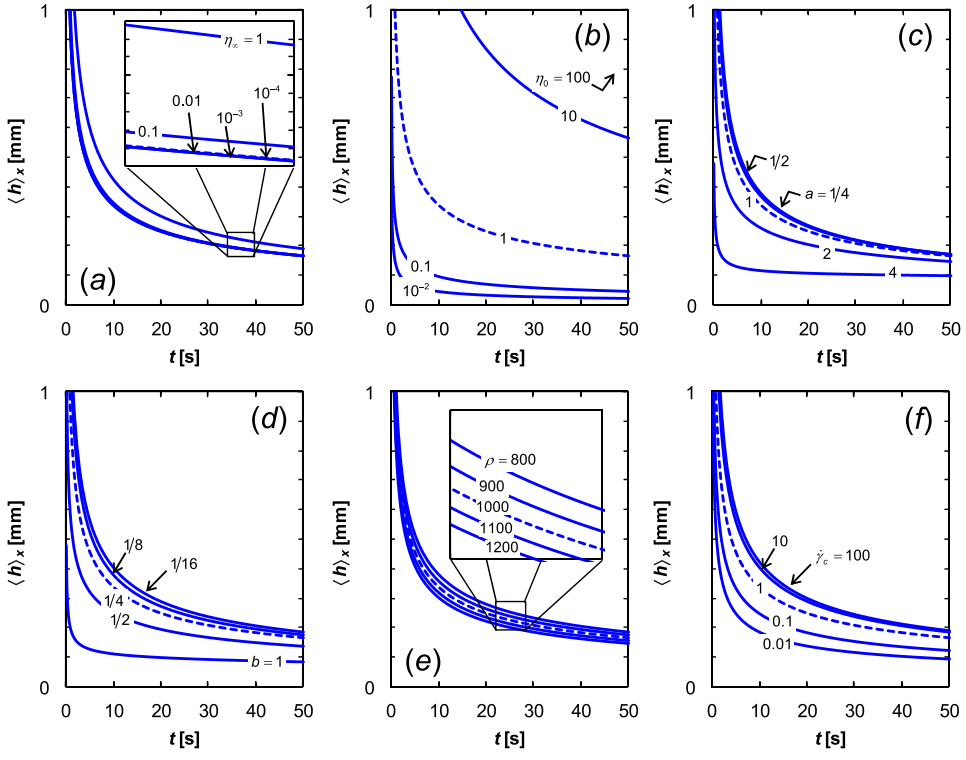

Fig. 7. Averaged film thickness as a function of draining time for selected values of (a) η_∞, (b) η_0, (c) a, (d) b, (e) ρ, and (f) $\dot{\gamma}_c$. Dashed lines represent a reference condition with $\eta_\infty = 10^{-2}$ Pa s, $\eta_0 = 1$ Pa s, $a = 1$, $b = 1/4$, $\rho = 1000\ \text{kg m}^{-3}$, and $\dot{\gamma}_c = 1\ \text{s}^{-1}$.

for the later parameter. On the other hand, increments in η_∞/η_0 produces more concave profiles and higher values of Q^* (Fig. 5c). At extreme cases, Eq. (24) predicts $Q^* \to 1$ as $\eta_\infty/\eta_0 \to 1$ and $Q^* = (1-Z_m)^{2b}{}_2F_1(1,2b;1+\frac{3}{a};Z_m) - \frac{3ab}{3+a}Z_m(1-Z_m)^{2b}{}_2F_1(1,1+2b;2+\frac{3}{a};Z_m)$ when $\eta_\infty/\eta_0 \to 0$.

3.3.3. Local film thickness

Profiles of local film thickness h, predicted by Eq. (27), as a function of the space-time variable x/t for selected values of $\eta_\infty, \eta_0, a, b, \rho$, and $\dot{\gamma}_c$ are shown in Fig. 6. An increase in both η_∞ (Fig. 6a) and η_0 (Fig. 6b), produces an increase in local values of h. The effect of η_0 on the development of profiles is more pronounced than is the case of η_∞. This behavior occurs because the range of local viscosity values in film ranges from η_0 at the air-film interface (*i.e.* $\dot{\gamma}=0$) to η_m at the wall-film interface. The value of η_m is always greater than η_∞ and may or may not be close to η_∞ depending on the value of $\dot{\gamma}_c$ (Fig. 2). For the value of $\dot{\gamma}_c$ considered as reference (*i.e.* 1 s^{-1}), changes in η_∞ under 10^{-2} Pa s produce a negligible effect on h. The effect of a and b on h is similar in sign and magnitude (Fig. 6c,d). An increase in those parameters produces thinner films due to the corresponding relative less viscous fluids. Inversely proportional increments in local film thickness are observed in the case of ρ (Fig. 6e). As the film is denser, it becomes heavier per unit volume draining faster from the plate and producing thinner coatings. Finally, an increase in $\dot{\gamma}_c$ results in thicker films (Fig. 6f). Higher values of this parameter produces relatively more viscous fluids that drain slower from the plate.

3.3.4. Average film thickness

Fig. 7 shows the area-averaged film thickness as a function of time for a plate length of $x=L$ and selected values of η_∞, η_0, a, b, ρ, and $\dot{\gamma}_c$. Generally, Eq. (30) (combined with Eq. (27)) predicts a hyperbolic functionality of the type $\langle h\rangle_x = ct^{-d}$ where $c, d \geqslant 0$. This feature was observed in previous studies using other rheological models for pseudoplastic fluids and dispersions (Peralta et al., 2014a; Peralta and Meza, 2016). The effect of η_∞ and η_0 on $\langle h\rangle_x$ is similar to that observed for h (Fig. 6a,b). That is, higher values of these parameters produce a more viscous fluid and thicker films. Also, profiles were more affected by η_0 and values of η_∞ greater than 1 Pa s. Fig. 7c,d show similar inverse effect of a and b on thickness profiles. In case of density, heavier (high values of ρ) films produce thinner films with even distribution. Finally, as in the case of h, higher values of $\dot{\gamma}_c$ results in thicker films. In this case, an asymptotic behavior is observed for values $\dot{\gamma}_c \geqslant 100$.

Film uniformity was calculated as $\langle h\rangle_x/h$ and is shown in Fig. 8 as a function of Z_m for selected values of a, b, and η_∞/η_0. In general, an increase in Z_m produces more uniform (*i.e.* leveled) films. That is, higher values of $\dot{\gamma}_m$ may indicate (1) thicker films, (2) less viscous films or (3) a combination of both. On one hand, parameters a and b shown similar effect on uniformity profiles. An increase in both of them produced more uniform films. Nevertheless, for any given value of Z_m, more leveled films are obtained by an increment in b compared with a. In general, higher values of a and b produce relative less viscous fluids for a given film thickness, resulting in higher $\dot{\gamma}_m$ and consequently more uniform films. On the other hand, an increment in η_∞/η_0 results in less uniform films. That is, the film is less likely to comply to stresses due to a relatively higher viscosity.

A presence of extrema is observed in the profiles of Fig. 8 for high values of Z_m. These extrema can be found by differentiating Eq. (30) with respect to Z_m and equating to zero to yield:

$$\begin{aligned}&\left[(1-\eta_c)(1-Z_{me})^b{}_2F_1\left(1,2b;\frac{3}{a}+1;Z_{me}\right)\right.\\&\left.+2\eta_c{}_2F_1\left(1,b;\frac{3}{a}+1;Z_{me}\right)\right]\\&\left[(1-\eta_c)(1-Z_{me})^b(2abZ_{me}-3)-3\eta_c\right]\\&+9\eta_c(1-\eta_c)(1-Z_{me})^b\\&+3(1-\eta_c)^2(1-Z_{me})^{2b}+2\eta_c^2(3+abZ_{me})=0\end{aligned} \tag{34}$$

where Z_{me} is the normalized and dimensionless shear rate parameter that produces a maximum in uniformity ($\langle h\rangle_x/h$) through Eq. (30). Briefly, the existence of these extrema is mainly due to the different impact that changes in η have on the relative growth of the $\langle h\rangle_x$ and h profiles as a function of Z_m. As can be inferred from Eq. (30), Z_{me} can be found for $\dot{\gamma}$ values in the range associated with the beginning of the second Newtonian plateau (*i.e.* $\eta \to \eta_\infty$). Prior to this zone, increments in $\dot{\gamma}$ reduce largely the viscosity (see Fig. 2) producing a flattening effect on thickness profiles due to the increased fluidity. This phenomenon affects first h and second $\langle h\rangle_x$, giving a positive slope in $\langle h\rangle_x/h$. After Z_{me}, the viscosity tends to be a constant and the growth of both profiles stabilizes, recovering the tendency of a Newtonian behavior ($\langle h\rangle_x/h \to 2/3$).

3.4. Carreau model

As stated before, Eq. (9) can be simplified into several well-known rheological models. Analytical solutions to the main fluid-dynamic variables were already found and presented for some of these models in previous studies (*i.e.* Cross, Bingham, and Ostwald-deWaele) (Peralta et al., 2014a; Peralta and Meza, 2016). Those solutions were found by using some of the helpful equalities (or a combination of them) presented elsewhere (Weisstein,

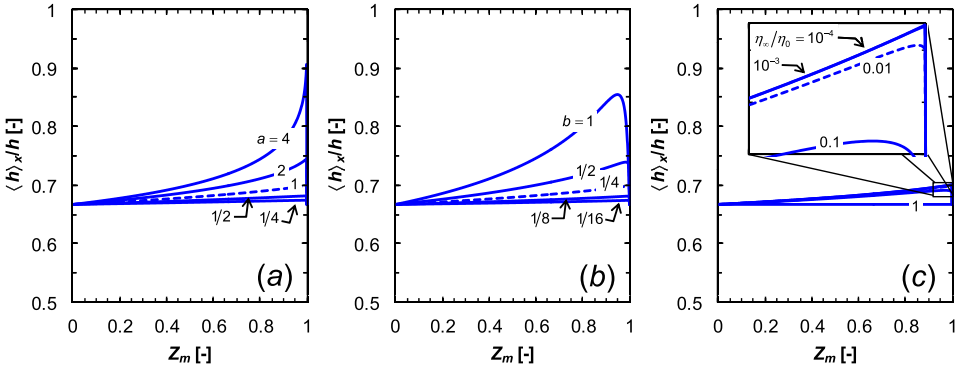

Fig. 8. Film uniformity ($\langle h\rangle_x/h$) as a function of the normalized and dimensionless shear rate parameter for selected values of: (a) a, (b) b, and (c) η_∞/η_0. Dashed lines represent a reference condition with $a=1$, $b=1/4$, and $\eta_\infty/\eta_0=0.01$.

2016a; Weisstein, 2016b). Nevertheless, no analytical solutions for a draining system using a Carreau fluid (*i.e.* $a = 2$ in Eq. (9)) were found in the literature. This model is extensively used in a wide range of disciplines, from technicians to researchers. Thus, taking into account the importance of the Carreau model, the following novel expressions correspond to the main fluid-dynamic variables using that model:

$$\psi(\dot{\gamma}_m) = \frac{Z_m}{1-Z_m}\left\{\eta_c + (1-\eta_c)(1-Z_m)^b\left[2 - \frac{(1-Z_m)^b + Z_m - 1}{(1-b)Z_m(1-Z_m)^b}\right]\right\} \tag{35}$$

$$\psi(\dot{\gamma}) = \frac{Z}{1-Z}\left\{\eta_c + (1-\eta_c)(1-Z)^b\left[2 - \frac{(1-Z)^b + Z - 1}{(1-b)Z(1-Z)^b}\right]\right\} \tag{36}$$

$$\frac{y}{h} = 1 - \frac{\left[\eta_c + (1-\eta_c)(1-\xi Z_m)^b\right]\xi^{1/2}(1-Z_m)^{1/2}}{\left[\eta_c + (1-\eta_c)(1-Z_m)^b\right](1-\xi Z_m)^{1/2}} \tag{37}$$

$$\begin{aligned} Q = \frac{\eta_0^2\dot{\gamma}_m^3}{3(\rho g_x)^2}\Bigg[&\eta_c^2 + \frac{2\eta_c(1-\eta_c)}{(1-Z_m)^{-b}}{}_2F_1\left(1,b;\frac{5}{2};Z_m\right) \\ &+ \frac{(1-\eta_c)^2}{(1-Z_m)^{-2b}}{}_2F_1\left(1,2b;\frac{5}{2};Z_m\right) \\ &- \frac{6}{5}\frac{b\eta_c(1-\eta_c)Z_m}{(1-Z_m)^{-b}}{}_2F_1\left(1,b+1;\frac{7}{2};Z_m\right) \\ &- \frac{6}{5}\frac{b(1-\eta_c)^2Z_m}{(1-Z_m)^{-2b}}{}_2F_1\left(1,2b+1;\frac{7}{2};Z_m\right)\Bigg] \end{aligned} \tag{38}$$

$$\left[h^2 + \frac{(x/t)^2}{\dot{\gamma}_c^2}\right]^b \frac{\rho g_x h^2}{(x/t)} - \left[h^2 + \frac{(x/t)^2}{\dot{\gamma}_c^2}\right]^b \eta_\infty - (\eta_0 - \eta_\infty)h^{2b} = 0 \tag{39}$$

$$\begin{aligned} \frac{\langle h\rangle_x}{h} = &\frac{1}{\left[\eta_c + (1-\eta_c)(1-Z_m)^b\right]^2} \\ &\Bigg[\frac{2}{3}\eta_c^2 + \frac{4}{3}\frac{\eta_c(1-\eta_c)}{(1-Z_m)^{-b}}{}_2F_1\left(1,b;\frac{5}{2};Z_m\right) \\ &+ \frac{2}{3}\frac{(1-\eta_c)^2}{(1-Z_m)^{-2b}}{}_2F_1\left(1,2b;\frac{5}{2};Z_m\right) \\ &- \frac{2}{5}\frac{b(1-\eta_c)^2Z_m}{(1-Z_m)^{-2b}}{}_2F_1\left(1,2b+1;\frac{7}{2};Z_m\right) \\ &- \frac{2}{5}\frac{b\eta_c(1-\eta_c)Z_m}{(1-Z_m)^{-b}}{}_2F_1\left(1,b+1;\frac{7}{2};Z_m\right)\Bigg] \end{aligned} \tag{40}$$

To calculate v_x, Eqs. (35)–(37) should be used with Eq. (18).

4. Conclusions

A mathematical model and its analytical solutions for the fluid-dynamic variables of a free-draining flow during a dip-coating draining stage of a finite vertical plate were obtained in this study. A fluid whose rheological behavior is described by the Carreau-Yasuda model was considered as part of the theoretical approach. The proposed expressions have been obtained assuming a monophasic, isothermal, and nonevaporative system, where the highest forces are viscous and gravitational. The studied phenomena occur far away from the meniscus formed at the surface of the fluid reservoir. The main operative variables estimated are the velocity profile (Eqs. (18)–(21)), flow rate (Eq. (24)), local thickness (Eq. (27)), and average thickness (Eq. (30)) of the film. Finally, a validation was performed (prediction errors < 15%) by using experimental data of average film thickness values of several representative food-grade fluids with coating capacity (cream, condensed sweet milk, microparticulated whey protein suspension, glaze suspension, milk chocolate, and deep-fat frying batters) obtained from the literature (Table 1).

The information published in this work will be useful for researchers and technicians to control and predict both film characteristics (such as thickness and uniformity) and operational variables (velocity, flow rate, etc.) during laboratory and industrial coating processes where free-draining flow takes place. This way, a practical application by decreasing trial-and-error predictions is also expected.

Acknowledgement

This research was supported partially by Universidad Nacional del Litoral (projects CAI+D: 501 201101 00031 LI, 501 201101 00088 LI and 501 201101 00156 LI) (Santa Fe, Argentina), Consejo Nacional de Investigaciones Científicas y Técnicas (Argentina), Agencia Nacional de Promoción Científica y Tecnológica (projects ANPCyT: 2011-182 and 2012-1413) (Argentina), and Secretaría de Estado de Ciencia, Tecnología e Innovación (project SECTEI: 2010-010-14) (Santa Fe, Argentina).

References

Ali, A., Underwood, A., Lee, Y.-R., Wilson, D., 2016. Self-drainage of viscous liquids in vertical and inclined pipes. Food Bioprod. Process. 99, 38–50.
Bingham, E.C., 1922. Fluidity and Plasticity. McGraw-Hill.
Brummer, R., 2006. Rheology Essentials of Cosmetic and Food Emulsions. Springer, Berlin; London.
Carreau, P.J., 1972. Rheological equations from molecular network theories. J. Rheol. (Melville, NY, US) 16 (1), 99.
Cross, M.M., 1965. Rheology of non-Newtonian fluids: a new flow equation for pseudoplastic systems. J. Colloid Sci. 20 (5), 417–437.
Dantzig, J.A., Tucker, C.L., 2001. Modeling in Materials Processing. Cambridge University Press, Cambridge, England; New York.
Eley, R.R., Schwartz, L.W., 2002. Interaction of rheology, geometry, and process in coating flow. J. Coat. Technol. 74 (9), 43–53.
Genovese, D.B., 2012. Shear rheology of hard-sphere, dispersed, and aggregated suspensions, and filler-matrix composites. Adv. Colloid Interface Sci., 1–16
Gutfinger, C., Tallmadge, J.A., 1965. Films of non-Newtonian fluids adhering to flat plates. AIChE J. 11 (3), 403–413.
Javidi, M., Hrymak, A.N., 2015. Numerical simulation of the dip-coating process with wall effects on the coating film thickness. J. Coat. Technol. Res. 12 (5), 843–853.
Karnjanolarn, R., Mccarthy, K.L., 2006. Rheology of different formulations of milk chocolate and the effect on coating thickness. J. Texture Stud. 37 (6), 668–680.
Kistler, S.F., Schweizer, P.M., 1997. Liquid Film Coating Scientific Principles and Their Technological Implications. Springer, Netherlands, Dordrecht.
Lapasin, R., Pricl, S., 1995. Rheology of Industrial Polysaccharides: Theory and Applications. Springer US: Imprint: Springer, Boston, MA.
Lee, S., Ng, P., Steffe, J., 2002. Effects of controlled mixing on the rheological properties of deep-fat frying batters at different percent solids. J. Food Process Eng. 25 (5), 381–394.
Meza, B.E., Peralta, J.M., Zorrilla, S.E., 2015. Rheological properties of a commercial food glaze material and their effect on the film thickness obtained by dip coating: rheology of food glaze and film thickness. J. Food Process Eng. 38 (5), 510–516.
Morrison, F.A., 2013. An Introduction to Fluid Mechanics. Cambridge University Press, Cambridge; New York.
Osswald, T., Rudolph, N., 2014. Polymer Rheology: Fundamentals and Applications. Hanser, Munich Cincinnati.
Ostwald, W., 1925. Ueber die Geschwindigkeitsfunktion der viskositat disperser systeme I. Kolloid-Z 36, 99–117.
Peralta, J.M., Meza, B.E., 2016. Mathematical modeling of a dip-coating process using concentrated dispersions. Ind. Eng. Chem. Res. 55 (34), 9295–9311.
Peralta, J.M., Meza, B.E., Zorrilla, S.E., 2014a. Mathematical modeling of a dip-coating process using a generalized Newtonian fluid. 1. Model development. Ind. Eng. Chem. Res. 53 (15), 6521–6532.
Peralta, J.M., Meza, B.E., Zorrilla, S.E., 2014b. Mathematical modeling of a dip-coating process using a generalized Newtonian fluid. 2. Model validation and sensitivity analysis. Ind. Eng. Chem. Res. 53 (15), 6533–6543.
Quemada, D., 1998. Rheological modelling of complex fluids. I. The concept of effective volume fraction revisited. Eur. Phys. J.: Appl. Phys. 1 (1), 119–127.
Rao, M.A., 2014. Rheology of Fluid, Semisolid, and Solid Foods: Principles and Applications. Springer, New York.

Schunk, P.R., Hurd, A.J., Brinker, C.J., 1997. Free-meniscus coating processes. In: Kistler, S.F., Schweizer, P.M. (Eds.), Liquid Film Coating. Scientific principles and their technological implications. Springer, Netherlands, Dordrecht, pp. 673–708.

Sherwood, J.D., 2009. Optimal shapes for best draining. Phys. Fluids 21 (11), 113102.

Sochi, T., 2015. Analytical solutions for the flow of carreau and cross fluids in circular pipes and thin slits. Rheol. Acta 54 (8), 745–756.

Spikes, H., Jie, Z., 2014. History, origins and prediction of elastohydrodynamic friction. Tribol. Lett. 56 (1), 1–25.

Surana, K.S., 2014. Advanced Mechanics of Continua. Applied and computational mechanics series. CRC Press, Boca Raton.

Tallmadge, J.A., Gutfinger, C., 1967. Entrainment of liquid films: drainage, withdrawal, and removal. Ind. Eng. Chem. 59 (11), 18–34.

Ungarish, M., Sherwood, J.D., 2012. Draining of a thin film on the wall of a conical container set into rapid rotation about its vertical axis. Phys. Fluids 24 (2), 023602.

Weinstein, S.J., Palmer, H.J., 1997. Capillary hydrodynamics and interfacial phenomena. In: Kistler, S.F., Schweizer, P.M. (Eds.), Liquid Film Coating Scientific Principles and Their Technological Implications. Springer, Netherlands, Dordrecht, pp. 19–62.

Weisstein, E.W., 2016a. Gauss Hypergeometric Function 2f1. <Http://functions.wolfram.com/HypergeometricFunctions/Hyper-geometric2F1> (accessed Jul 1, 2016).

Weisstein, E.W., 2016b. Incomplete Beta Function. <Http://mathworld.wolfram.com/IncompleteBetaFunction.html> (accessed Jul 1, 2016).

Willenbacher, N., Georgieva, K., 2013. Rheology of disperse systems. In: Brockel, U., Meier, W., Wagner, G. (Eds.), Product Design and Engineering. Wiley-VCH Verlag GmbH & Co. KGaA, Weinheim, Germany, pp. 7–49.

Yasuda, K., 1979. Investigation of the Analogies Between Viscometric and Linear Viscoelastic Properties of Polystyrene Fluids. Ph.D., Massachusetts Institute of Technology, Dept. of Chemical Engineering, Boston.

Zhang, X.-M., Chen, M.-M., Ma, J.-P., Chen, W.-X., Feng, L.-F., 2016. Numerical simulation and experimental validation of liquid-film-flow characteristics in dip coating for non-Newtonian fluids. Polym. Eng. Sci. 56 (9), 1070–1078.